Experimental Validation of Scalable Electromagnetically-Modeled RIS Through Ray Tracing and Indoor Measurements

Le Hao [*], Sravan K. R. Vuyyuru [†‡], Sergei A. Tretyakov [†], and Risto Valkonen [‡]
[*]Institute of Telecommunications, TU Wien, Vienna, Austria
[†]Department of Electronics and Nanoengineering, School of Electrical Engineering, Aalto University, 02150 Espoo, Finland
[‡]Nokia Bell Labs, Karakaari 7, 02610 Espoo, Finland
(Emails: [*]*le.hao@tuwien.ac.at*, [†]*sravan.vuyyuru@aalto.fi*)

***Abstract*—This work focuses on integrating electromagnetically consistent modeling of scalable anomalous reflectors into the design and optimization of future wireless networks. A manufactured anomalous reflector sample is utilized to validate various path loss models for reconfigurable intelligent surface (RIS)-assisted links through theoretical analysis, ray tracing simulation, and measurements. A static anomalous reflector prototype is developed for testing based on a linear periodic 'supercell' design, accounting for intrinsic losses and mutual coupling of RIS unit cells, then scaled to a medium-sized square planar array. To accurately model RIS in ray tracers, the radiation patterns are imported from electromagnetic solver simulations. The measurement results agree with ray tracing simulations and validate the developed models. The proposed models and methods of RIS-link analysis are adaptable to other RISs and compatible with different ray tracers, potentially reducing the need for massive calibration measurements.**

***Index Terms*—Anomalous reflector, measurement, ray tracing, reconfigurable intelligent surface (RIS), 6G.**

I. Introduction

In recent years, reconfigurable intelligent surfaces (RISs) have been broadly studied as a potential key technology in the next generation of wireless communication systems [1]. RIS technologies offer potential advantages of low cost compared to traditional antenna technologies such as massive multiple-input multiple-output (MIMO) and relays since they function as nearly passive devices [2]. A RIS as an anomalous reflector (AR) comprising discrete tunable elements allows steering the reflected beam toward any desired direction [3]–[7], increasing the signal power at target locations while mitigating interference in unwanted directions.

To realize the AR functionality with RIS technology for real-world deployment, its electromagnetic (EM) properties have to be studied and then modeled with sufficient accuracy. From the EM perspective, directional scattering patterns and reflection efficiency are important parameters for assessing RIS performance, and linking the EM theory with the communication theory, allowing the evaluation of factors such as large-scale fading and the power received through the RIS [8]. The Floquet-Bloch theory is commonly used to design RIS as periodical structures [3]. Based on scattering synthesis for periodically loaded patch arrays [4], a novel approach has been introduced for designing high-efficiency wide-angle anomalous reflectors, bypassing the need for resource-intensive full-wave EM simulations. We utilized this method to develop anomalous reflectors in [5], and here we focus on integrating models of RIS EM properties into a ray tracer, verifying the simulation results by measurements. The results allow us to effectively evaluate RIS performance in realistic environments.

The state-of-the-art of relevant studies include a macroscopic model for evaluating the multimode re-radiation and diffuse scattering from a RIS [9], later incorporating metasurface scattering at different points of the interaction chain, with ray-tracing simulations conducted in an indoor scenario for lossy, phase-gradient AR [10]. In addition, system-level simulations have been carried out in [11] to evaluate the system performance of RIS-assisted networks. Furthermore, a comprehensive overview of RIS-based channel measurements, including large- and small-scale fading in RIS-assisted wireless communication systems, is provided in [12]. However, existing research often focuses either on EM or the communication aspect, lacking a unified approach. This paper aims to build a connection between the EM and communication perspectives, enabling a comprehensive analysis of RIS communication performance based on the EM theory while minimizing the need for extensive measurements.

II. EM-Consistent Modeling of Anomalous Reflectors: Scalable Design and Manufactured Static Test AR

Using the technique presented in [5], we have developed a scalable AR in order to test the integration of its EM properties models with ray-tracing communication models, allowing studies of link performance. An algebraic scattering synthesis [4] is used to optimize the scattering behavior of loaded periodic patch arrays. The supercell-level synthesis of load reactances accelerates the design and avoids intensive EM simulations for scattering optimizations.

A flat 16-element supercell structure, linearly arranged in the x-dimension, is designed to steer normally incident waves into nine anomalous directions, supported by perfect match

978-88-31299-10-7/25/$31.00 ©2025 IEEE

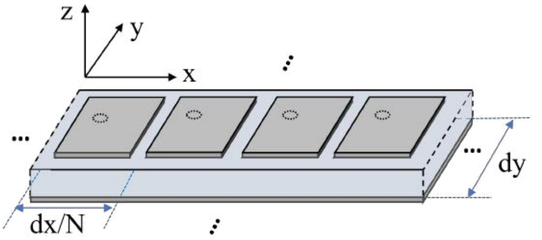

(a) Supercell structure of the designed AR consisting of N elements.

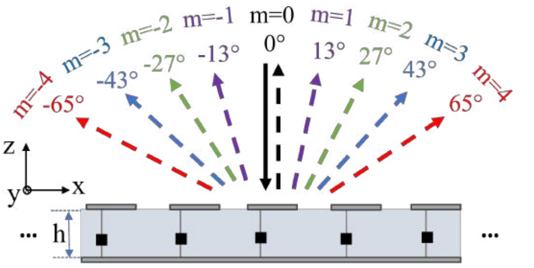

(b) Illustration of the incidence wave and reflection waves at different propagating harmonics.

Figure 1: The structure and propagation harmonics of the designed AR.

TABLE I: Dimensions of the supercell array

Parameters	dimensions
Supercell dimension	$4.4135\lambda \times 0.2758\lambda$
Unit cell dimension	$0.2758\lambda \times 0.2758\lambda$
Patch dimension	$0.2068\lambda \times 0.2068\lambda$
Substrate height	0.52 mm
Probe feed position	$(0, 1.11)$ mm

to propagating Floquet harmonics up to the fourth order, as illustrated in Fig. 1. These nine propagating harmonics correspond to reflection directions $\theta_r = 0°, \pm 13°, \pm 27°, \pm 43°$, and $\pm 65°$ with $\phi_r = 0°$, as defined by the Floquet expansion. The supercell periodicity is determined by $4\lambda / \sin\theta_{r,max}$, where $\theta_{r,max}$ is the maximum desired reflection angle. While the simulation is performed for supercell design with infinite periodic boundary conditions, the scattering characteristics are approximated to synthesize the finite-sized reflector consisting of 48×48 unit cells, i.e. 48×3 supercells.

Following the manufacturing technique proposed in [7], a compact static 26 GHz AR prototype, designed to deflect into $+65°$ under normal incidence, was made. Figure 2 shows the manufactured prototype, consisting of an array of 48×48 square-shaped unit cells, with an overall dimension of $13.24\lambda \times 13.24\lambda$. The array is manufactured on a dual-layer printed circuit board (PCB), using a Rogers RO4350B laminate ($\epsilon_r = 3.55$, $\tan\delta = 0.0037$, a 0.52-mm thickness). A 3-bit quantized implementation of reactive load resolution is used, realizing 8 different reflection phase responses with a $45°$ step in the $[0°\ 360°]$ range. This selection of load quantization offers a favorable tradeoff between performance and complexity, based on the analysis in [5]. The EM performance of the manufactured AR prototype is verified through measurements conducted in an anechoic chamber, confirming that the measured scattering pattern of the AR matches the CST simulation results, particularly in the desired reflection direction. In the subsequent sections, we use this AR prototype as a test RIS example to analyze the connection between EM properties and communication performance.

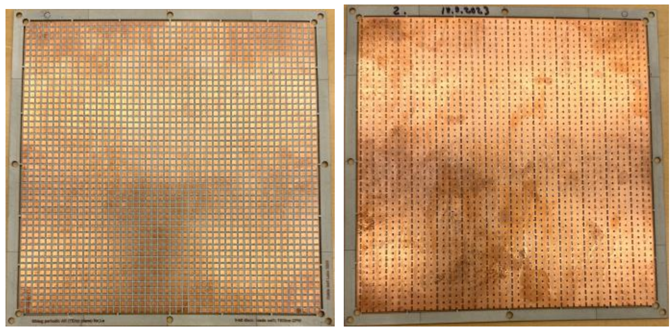

(a) Front side. (b) Back side.

Figure 2: A manufactured 48×48-sized anomalous reflector.

III. Path Loss Models for RIS-Assisted Links

We use two different EM-consistent theoretical models for calculating the path gain of an RIS-assisted link. Model 1 is obtained from [13], based on the RIS geometrical area and the angles of arrival and reflection. It calculates the far-field received power at the receiver (Rx) side through a perfectly functioning AR as

$$P_1 = P_t G_t G_r \eta_{\text{eff}} \left(\frac{S_1}{4\pi d_t d_r} \right)^2 |\cos\theta_i \cos\theta_r|, \quad (1)$$

where P_t is the transmitted power, G_t and G_r are the angle-dependent Tx and Rx antenna gains, and η_{eff} accounts for losses from RIS imperfections. The geometrical area of the RIS panel is denoted as S_1; d_t and d_r represent the distances between the Tx and RIS, and RIS and Rx, respectively. This model considers an ideal setup, where the RIS is optimized to provide anomalous reflection towards the user at θ_r from the incident waves at θ_i. The angles are counted from the normal direction to the RIS plane.

The second analytical model incorporates the EM-simulated receiving and transmitting scattering patterns of the RIS. The received power is written as

$$P_2 = \frac{P_t G_t G_r G_{\text{tx}} G_{\text{rx}} \lambda^4}{(4\pi)^4 (d_t d_r)^2} \eta_{\text{eff}}, \quad (2)$$

where the parameters G_t, G_r, d_t, d_r and η_{eff} are the same as in model 1. G_{rx} and G_{tx} represent the angle-depended RIS gains in the direction from RIS to Tx and RIS to Rx, respectively. Both RIS gains are computed using the directivity patterns obtained from simulations in CST Microwave Studio. Both theoretical path loss models align when the designed anomalous reflector achieves near-perfect efficiency.

These two models only calculate the free space path loss for a Tx-RIS-Rx link. In a real environment, waves from Tx can reach Rx also via reflection and scattering by other objects. Ray tracing effectively incorporates these propagation effects in models of complex environments. Therefore, in addition to the RIS models, we use the MATLAB ray tracer to calculate the received power when RIS is used in complex environments. Since MATLAB cannot directly model a cascaded Tx-RIS-Rx link, we simulate the Tx-RIS and RIS-Rx links separately. Firstly, we import the RIS radiation pattern towards the Tx antenna, i.e., at $0°$, and model the RIS as a receiving antenna. The path loss from Tx to the RIS is denoted as L_t, and the received power at the RIS is calculated as $P_{r1} = P_t/L_t$. Next, we import the RIS pattern towards the Rx antenna, i.e., at $65°$, and model the RIS as a transmitting antenna, with the transmitted power equal to the RIS received power P_{r1}. The path loss from the RIS to the Rx is denoted as L_r. The final received power at the Rx antenna is calculated as

$$P_3 = \frac{P_{r1}}{L_r} = \frac{P_t}{L_t L_r} \tag{3}$$

It should be noted that the path losses L_t and L_r take into account the radiation patterns of the RIS, Tx, and Rx antennas. They also include line-of-sight (LOS), non-line-of-sight (NLOS) paths, and reflection losses for each path. When only one LOS path exists for Tx-RIS and RIS-Rx links, the Eq. (3) is equivalent to Eq. (2) since only the free space path loss is calculated. More details of path loss calculations in the MATLAB ray tracer can be found in [14].

IV. Indoor measurement with the AR

In this section, we perform measurements in a $14 \times 8 \times 3$ (m)^3 sized room, as shown in Fig. 3. The Tx and Rx antennas are identical horn antennas, each with the maximum gain of $G_t = G_r = 18$ dBi at 26 GHz. The Tx antenna is connected to a vector signal generator (VSG) via a cable with the loss of $L_c = 2.5$ dB. The output power from the VSG is $P_t = 6$ dBm. The VSG generates a 5G NR PUSCH signal within a channel bandwidth of 400 MHz for 16 quadrature amplitude modulation (QAM) orthogonal frequency-division multiplexing (OFDM) modulation scheme. The Rx antenna is connected to a low-noise-amplifier (LNA) and subsequently connected to a vector signal analyzer (VSA) via cables. The Rx cable loss together with the LNA gain is $G_a = 19.9$ dB. The Tx and AR are positioned at the distance $d_t = 5.5$ m, while the Rx antenna is placed at seven angles: $55°$ to $85°$ with a $5°$ step from the AR, maintaining a consistent $d_r = 7$ m distance. All antennas (Tx, Rx, AR) are mounted on tripods at the same height of 1.5 m.

To evaluate the accuracy of our theoretical models with the RIS, we compare measurement results with theoretical predictions. However, slight discrepancies may arise due to measurement device-specific variations, such as fluctuations in LNA gain from temperature changes. To eliminate the influence of such factors and make a fair comparison, we first perform a LOS link measurement with only the Tx and Rx antennas and without the AR, establishing a reference comparison between the measured and theoretical results in such a simple scenario. In this measurement, we fix the Tx location and place the Rx antenna at 7 different positions to measure the received power and error vector magnitude (EVM). The EVM is a parameter that indicates the received signal quality throughout the measured channel bandwidth for evaluating the conditions of the received signal demodulation. Every time when we change the Rx position, we adjust the Tx and Rx antenna so that their centers are aligned. The measured received powers at 26 GHz for the seven locations are denoted as $\mathbf{p}_{\text{m,LOS}}$. Note that we use non-boldface letters to denote scalars and lowercase boldface letters to denote vectors in this work.

We determine the free space path loss between the Tx and the Rx at the 7 locations using the Friis formula

$$\mathbf{p}_{\text{FSPL}} = 10 \log_{10} \left(\frac{\lambda}{4\pi \mathbf{d}} \right)^2, \tag{4}$$

in dB, where $\mathbf{d} = [5.88, 6.25, 6.79, 7.27, 7.70, 8.10, 8.42]$ (m) denotes the 7 distances between the Tx and the Rx antenna corresponding to the 7 angles. The final calculated received power from theory is

$$\mathbf{p}_{\text{theory}} = P_t + G_t + G_r + \mathbf{p}_{\text{FSPL}} - L_c + G_a \tag{5}$$

in dBm. The power difference between the theoretical and measured results is

$$\mathbf{p}_{\text{diff}} = \mathbf{p}_{\text{theory}} - \mathbf{p}_{\text{m,LOS}} \tag{6}$$

in dB. The values of the $\mathbf{p}_{\text{diff}}$ are listed in Table II, and they are very small. Next, we can use this vector to calibrate our theoretical calculations and ray tracing simulations for the AR-assisted link to obtain more accurate results.

TABLE II: Power differences between theory and measurements

Angle	$55°$	$60°$	$65°$	$70°$	$75°$	$80°$	$85°$
$\mathbf{p}_{\text{diff}}$ (dB)	1.46	1.55	1.08	0.68	0.26	1.05	0.28

We then repeat the measurements using the AR, keeping the Tx and Rx antennas aligned with the AR's center at each Rx position. A microwave absorber blocks the LOS path. Seven power measurements are collected, denoted as $\mathbf{p}_{\text{m}}$.

V. Theoretical analysis and ray tracing simulation with the AR

To test the AR with the path loss models explained in Sec. III, we apply the same parameter values as in the measurement for all models, including P_t, G_t, G_r, d_t, and d_r. The AR's geometrical area as equals $S_1 = 152.6$ mm$\times$152.6 mm. We set $\eta_{\text{eff}} = 1$ assuming perfect anomalous reflections without loss, $\theta_i = 0°$, and $\theta_r = 65°$. With model 1, we obtain a single scalar power value at $65°$ for 26 GHz since the AR is designed for this angle and frequency. With model 2, the G_{tx} and G_{rx} obtained from CST simulations are listed in Table III.

Figure 3: The indoor measurement scenario with an auditorium setting, using a 48×48-sized AR.

TABLE III: RIS GAIN VALUES

Angle	55°	60°	65°	70°	75°	80°	85°	0°
G_{tx} (dB)	12.90	25.61	29.42	25.58	15.47	−1.95	8.61	
G_{rx}(dB)								33.11

For the ray-tracing model, we replicate the measurement scenario into a 3D model, as shown in Fig. 4(a) and import it into the MATLAB ray tracer for simulation. Two horn antennas with a maximum gain of 18 dBi at 26 GHz are modeled as the Tx and Rx antennas. In addition, we import the simulated radiation patterns of the AR into the ray tracer, including the patterns towards the Tx and Rx antenna. Figure 4(b) shows the LOS paths for the Tx-AR and AR-Rx links in the ray tracer. The locations of the AR, Tx, and Rx antennas in the ray tracer are the same as in the measurements. We first run ray tracing simulations with zero reflection [Eq. (3)] to compare the results with model 1 [Eq. (1)] and model 2 [Eq. (2)] since they all consider only LOS paths. Next, we set a maximum of three reflections to compare the results with measurements.

After obtaining the theoretical and ray tracing simulation results, we perform a calibration step, i.e., use the $\mathbf{p}_{\text{diff}}$ vector to calibrate the obtained results. Since the measurements include the cable losses and LNA gains, the results from all the models must account for these factors. The final results from the two RIS models and the ray-tracing estimation are calculated as

$$\mathbf{p}_{m1} = \mathbf{p}_1 - L_c + G_a - \mathbf{p}_{\text{diff}}, \tag{7}$$

$$\mathbf{p}_{m2} = \mathbf{p}_2 - L_c + G_a - \mathbf{p}_{\text{diff}}, \tag{8}$$

and

$$\mathbf{p}_{m3} = \mathbf{p}_3 - L_c + G_a - \mathbf{p}_{\text{diff}}, \tag{9}$$

respectively. Here we use bold letters $\mathbf{p}_1$, $\mathbf{p}_2$, and $\mathbf{p}_3$ to represent the collected results at seven angles from the three models, respectively.

VI. Results comparison

In this section, we compare the calculated results $\mathbf{p}_{m1}$ from model 1, $\mathbf{p}_{m2}$ from model 2, ray tracing (RT) simulation results $\mathbf{p}_{m3}$, and the measurement results $\mathbf{p}_{\text{m}}$. The received powers from each method are compared in Table IV. We observe that model 2 and the ray-tracing model with zero reflections are identical, as both consider only a single LOS path from Tx to AR to Rx. Model 1 gives the highest power, because it represents the case of ideal RIS performance. However, by comparing it with the measured result at 65°, we see that the difference is only about 2.3 dB, suggesting

(a) A top view of the 3D indoor room model.

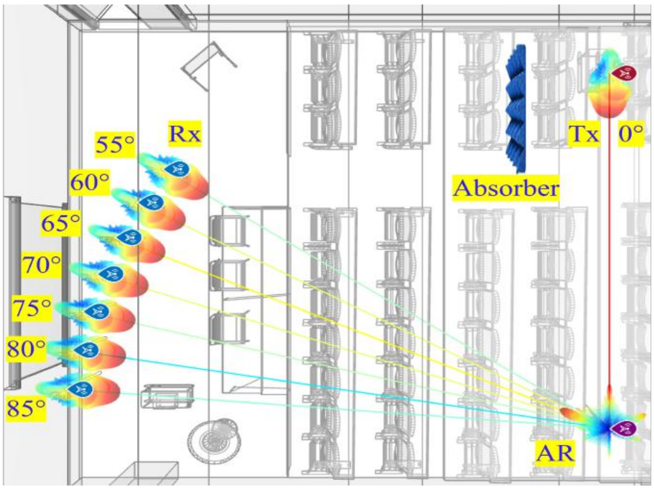

(b) The positions and radiation patterns of the Tx, Rx, and AR in the MATLAB ray tracer.

Figure 4: The 3D room model and LOS paths in the ray tracer.

TABLE IV: RECEIVED POWER COMPARISON

Angle	55°	60°	65°	70°	75°	80°	85°
Model 1			−31.67				
Model 2	−49.17	−36.55	−32.27	−35.70	−45.39	−63.60	−52.2
RT: 0 reflection	−49.13	−36.52	−32.23	−35.66	−45.37	−63.57	−52.24
RT: 3 reflection	−50.48	−37.86	−33.62	−36.97	−46.56	−68.76	−52.78
Measurement	−46.46	−37.70	−33.93	−36.80	−43.88	−48.53	−43.81

TABLE V: EVM RESULTS

Angle	55°	60°	65°	70°	75°	80°	85°
EVM	27.42	9.83	5.96	9.25	20.23	29.30	21.29

that our manufactured AR has moderate losses relative to the ideal lossless AR without parasitic scattering. In addition, the measured results are very close to the ray tracing simulation results with 3 reflections between 60° and 70°, which is the main reflection beam direction, with differences under 0.4 dB. This result demonstrates the accuracy of the ray tracing model with the AR in a 3D room setup. The slightly larger discrepancies at other angles are mainly due to the significant differences between the simulated and measured AR patterns at those angles, which is evident in Table III, where we see that the RIS gain at other angles is much smaller than its gain between 60° and 70°. Another possible reason for the discrepancies at those angles could be the reduced accuracy of the measurement results, as reflected in the measured EVM results listed in Table V. The EVM results between 60° and 70° are lower than 12.5%, which is the threshold to pass the frame-averaged EVM test with the 5G NR signal. The EVM values at other angles exceed the threshold, which implies that the measurement results at those angles are not very accurate. Therefore, the large differences between the measurement and simulation results at 55°, 75°, 80° and 85° do not necessarily mean our models are not robust, just the results between 60° and 70° are more reliable while the powers at the other angles are less accurate.

VII. Conclusion

In this work, we have described a manufactured AR that reflects normally incident plane waves toward 65° at 26 GHz designed using an array antenna scattering synthesis methodology to realize a perfect anomalous deflection. We have combined two EM models of RIS with a ray-tracing simulator to analyze received power through the Tx-AR-Rx link. These developed path loss models are validated through indoor measurements of received power, showing good agreement between the theoretical and simulated results at various angles. The proposed ray-tracing approach can be applied to other RISs or ARs and can be extended to outdoor or highly dynamic indoor environments, offering a cost-effective platform for predicting and analyzing communication performance without extensive measurements.

Acknowledgment

This work was partially funded by the European Union's Horizon 2020 research and innovation programme under the Marie Skłodowska-Curie grant agreement No. 956256, partially by the Research Council (Academy) of Finland with grant number 345178, by the Vienna Science and Technology Fund (WWTF) [Grant ID: 10.47379/VRG23002], and by the RCF-DoD Future Information Architecture for IoT initiative.

References

[1] M. Di Renzo, A. Zappone, M. Debbah, M.-S. Alouini, C. Yuen, J. de Rosny, and S. Tretyakov, "Smart radio environments empowered by reconfigurable intelligent surfaces: How it works, state of research, and the road ahead," *IEEE Journal on Selected Areas in Communications*, vol. 38, pp. 2450–2525, Nov. 2020.

[2] L.-H. Shen, K.-T. Feng, and L. Hanzo, "Five facets of 6g: Research challenges and opportunities," *ACM Comput. Surv.*, vol. 55, Feb. 2023.

[3] A. Díaz-Rubio and S. A. Tretyakov, "Macroscopic modeling of anomalously reflecting metasurfaces: Angular response and far-field scattering," *IEEE Transactions on Antennas and Propagation*, vol. 69, no. 10, pp. 6560–6571, 2021.

[4] S. K. R. Vuyyuru, R. Valkonen, D.-H. Kwon, and S. A. Tretyakov, "Efficient anomalous reflector design using array antenna scattering synthesis," *IEEE Antennas and Wireless Propagation Letters*, vol. 22, no. 7, pp. 1711–1715, 2023.

[5] S. K. R. Vuyyuru, L. Hao, M. Rupp, S. A. Tretyakov, and R. Valkonen, "Modeling RIS from Electromagnetic Principles to Communication Systems–Part I: Synthesis and Characterization of a Scalable Anomalous Reflector," *arXiv preprint arXiv:2403.12790*, 2024.

[6] D.-H. Kwon, "Lossless scalar metasurfaces for anomalous reflection based on efficient surface field optimization," *IEEE Antennas and Wireless Propagation Letters*, vol. 17, pp. 1149–1152, July 2018.

[7] S. K. R. Vuyyuru, R. Valkonen, S. A. Tretyakov, and D.-H. Kwon, "Efficient synthesis of large finite patch arrays for scanning wide-angle anomalous reflectors," *IEEE Open Journal of Antennas and Propagation*, 2024.

[8] L. Hao, F. S. Cuesta, and S. A. Tretyakov, "Comparison of simplistic system-level ris models and diffraction-theory solutions," in *2024 18th European Conference on Antennas and Propagation (EuCAP)*, pp. 1–5, 2024.

[9] V. Degli-Esposti, E. M. Vitucci, M. D. Renzo, and S. A. Tretyakov, "Reradiation and scattering from a reconfigurable intelligent surface: A general macroscopic model," *IEEE Transactions on Antennas and Propagation*, vol. 70, no. 10, pp. 8691–8706, 2022.

[10] E. M. Vitucci, M. Fabiani, and V. Degli-Esposti, "Use of a realistic ray-based model for the evaluation of indoor rf coverage solutions using reconfigurable intelligent surfaces," *Electronics*, vol. 12, no. 5, 2023.

[11] B. Sihlbom, M. I. Poulakis, and M. D. Renzo, "Reconfigurable intelligent surfaces: Performance assessment through a system-level simulator," *IEEE Wireless Communications*, pp. 1–10, 2022.

[12] J. Huang, C.-X. Wang, Y. Sun, R. Feng, J. Huang, B. Guo, Z. Zhong, and T. J. Cui, "Reconfigurable intelligent surfaces: Channel characterization and modeling," *Proceedings of the IEEE*, vol. 110, no. 9, pp. 1290–1311, 2022.

[13] S. Kosulnikov, F. S. Cuesta, X. Wang, and S. A. Tretyakov, "Simple link-budget estimation formulas for channels including anomalous reflectors," *IEEE Transactions on Antennas and Propagation*, vol. 71, pp. 5276–5288, June 2023.

[14] L. Hao, F. S. Cuesta, S. A. Tretyakov, and M. Rupp, "Improving propagation channels with static scatterers," *IEEE Antennas and Wireless Propagation Letters*, vol. 23, no. 6, pp. 1924 – 1928, 2024.